Tuning the Baird aromatic triplet-state energy of cyclooctatetraene to maximize the self-healing mechanism in organic fluorophores

Avik K. Pati[a,b], Ouissam El Bakouri[c,1], Steffen Jockusch[d,1], Zhou Zhou[a,1], Roger B. Altman[a,b], Gabriel A. Fitzgerald[a], Wesley B. Asher[e,f,g], Daniel S. Terry[a,b], Alessandro Borgia[b], Michael D. Holsey[e,f], Jake E. Batchelder[a,b], Chathura Abeywickrama[b], Brandt Huddle[a], Dominic Rufa[a], Jonathan A. Javitch[e,f,g], Henrik Ottosson[c], and Scott C. Blanchard[a,b,2]

[a]Department of Physiology and Biophysics, Weill Cornell Medicine, New York, NY 10065; [b]Department of Structural Biology, St. Jude Children's Research Hospital, Memphis, TN 38105; [c]Ångström Laboratory, Department of Chemistry, Uppsala University, Uppsala, 751 20 Sweden; [d]Department of Chemistry, Columbia University, New York, NY 10027; [e]Department of Psychiatry, Columbia University, New York, NY 10032; [f]Department of Pharmacology, Columbia University, New York, NY 10032; and [g]Division of Molecular Therapeutics, New York State Psychiatric Institute, New York, NY 10032

Edited by Taekjip Ha, Johns Hopkins University, Baltimore, MD, and approved August 17, 2020 (received for review April 7, 2020)

Bright, photostable, and nontoxic fluorescent contrast agents are critical for biological imaging. "Self-healing" dyes, in which triplet states are intramolecularly quenched, enable fluorescence imaging by increasing fluorophore brightness and longevity, while simultaneously reducing the generation of reactive oxygen species that promote phototoxicity. Here, we systematically examine the self-healing mechanism in cyanine-class organic fluorophores spanning the visible spectrum. We show that the Baird aromatic triplet-state energy of cyclooctatetraene can be physically altered to achieve order of magnitude enhancements in fluorophore brightness and signal-to-noise ratio in both the presence and absence of oxygen. We leverage these advances to achieve direct measurements of large-scale conformational dynamics within single molecules at submillisecond resolution using wide-field illumination and camera-based detection methods. These findings demonstrate the capacity to image functionally relevant conformational processes in biological systems in the kilohertz regime at physiological oxygen concentrations and shed important light on the multivariate parameters critical to self-healing organic fluorophore design.

self-healing fluorophore | photostability | Baird aromaticity | cyclooctatetraene | single-molecule imaging

Despite remarkable progress (1–5), fluorescence imaging pursuits, which are a central pillar of both medical and fundamental research, remain severely hampered by the limited durability and stochastic blinking of organic fluorophores. Such issues reduce photon budgets and signal-to-noise ratios, thereby compromising the information content of the experiments performed. Related considerations limit superresolution imaging methods (6), the temporal resolution that can be achieved when examining biological function, and the interpretation of dynamic processes within individual molecules at the single-molecule scale.

The performance of organic fluorophores in experimental settings is maximized when excitation-induced separation of valence electrons leads to reliable and repeated relaxation back to the ground state. Performance demands are particularly accentuated in single-molecule applications, where photon emission-induced relaxation must occur over millions of cycles, while nonfluorescent decay pathways must be minimized. The flux of photon emission in fluorescent species can be severely compromised when excited-state electrons undergo intersystem crossing to relatively long-lived, nonfluorescing triplet and radical states (Fig. 1*A*), whose lifetimes (*ca*. 100 μs to seconds) are orders of magnitude longer than singlet excited states (*ca*. 0.001 μs to 0.1 μs). Correspondingly, triplet states can dramatically reduce the number of detected photons per unit time (brightness). The relatively long lifetimes and high energies of triplet and radical states also render them prone to reactions with molecular oxygen, which can generate toxic reactive oxygen species (ROS). ROS include singlet oxygen, peroxide, and superoxide radicals that lead to chemical destruction of the fluorophore (photobleaching), photocrosslinking to elements in the surrounding environment, and other potentially toxic side effects (7–11).

Organic fluorophores commonly used in modern imaging applications (e.g., rhodamine- and cyanine-class fluorophores) typically exhibit relatively short excited-state lifetimes and low probabilities of intersystem crossing to triplet and radical states (13–15). Nonetheless, triplet and radical states can become significantly populated at elevated illumination intensities, an issue that is particularly problematic when imaging low-abundance species, including single-molecule and superresolution imaging applications (1–5, 11). In this regime, increasing illumination

Significance

Fluorescence imaging, a central pillar of medical and fundamental research, is hampered by stochastic blinking, limited photon budgets, and phototoxicities of organic fluorophores. Here, we use quantum chemical calculations and targeted synthetic strategies to tune the Baird aromatic triplet-state energy of cyclooctatetraene to enhance its capacity to mediate intramolecular triplet–triplet energy transfer with distinct organic fluorophores spanning the visible spectrum. By tuning the efficiency of the self-healing mechanism, we generate cyanine-class fluorophore derivatives with improved intrinsic brightness and photostability, and reduced reactive oxygen species generation. We leverage these advances to extend the time scale of camera-based, single-molecule imaging techniques, including Förster (fluorescence) resonance energy transfer methods, to the kilohertz regime in fully oxygenated physiological buffers.

Author contributions: A.K.P., O.E.B., S.J., R.B.A., W.B.A., D.S.T., J.A.J., H.O., and S.C.B. designed research; A.K.P., O.E.B., S.J., R.B.A., G.A.F., W.B.A., A.B., M.D.H., J.E.B., C.A., B.H., and D.R. performed research; Z.Z. and D.S.T. contributed new reagents/analytic tools; A.K.P., O.E.B., S.J., R.B.A., G.A.F., W.B.A., D.S.T., A.B., J.A.J., H.O., and S.C.B. analyzed data; and A.K.P., O.E.B., S.J., R.B.A., W.B.A., D.S.T., A.B., J.A.J., H.O., and S.C.B. wrote the paper.

Competing interest statement: S.C.B. and R.B.A. have an equity interest in Lumidyne Technologies.

This article is a PNAS Direct Submission.

[1]O.E.B., S.J., and Z.Z. contributed equally to this work.

[2]To whom correspondence may be addressed. Email: Scott.Blanchard@stjude.org.

This article contains supporting information online at https://www.pnas.org/lookup/suppl/doi:10.1073/pnas.2006517117/-/DCSupplemental.

First published September 10, 2020.

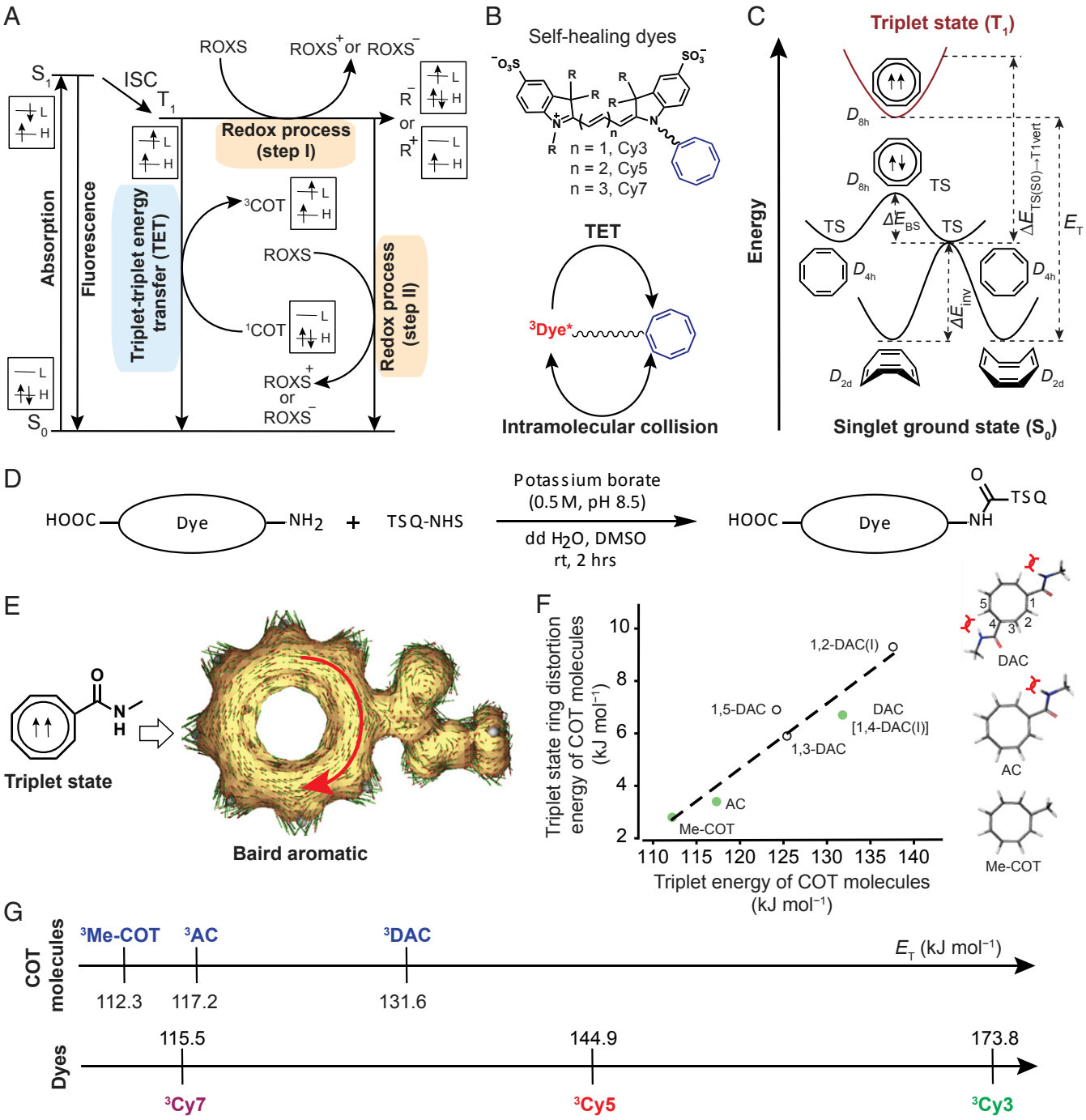

Fig. 1. Strategies for triplet-state quenching of organic fluorophores. (*A*) Simplified state energy diagram for fluorophore excitation and relaxation pathways including fluorophore's triplet-state quenching by small-molecule protective agents, such as COT and a combination of reducing and oxidizing species (ROXS). R^+, R^-, S_0, T_1, and ISC indicate radical cation, radical anion, singlet ground state, triplet state, and intersystem crossing of a fluorophore, respectively. The rectangular boxes show the electron and spin configurations for the corresponding states of a fluorophore and a COT molecule. H and L indicate highest occupied and lowest unoccupied molecular orbital, respectively. (*B*) Representative examples of self-healing organic fluorophores, in which a COT molecule is covalently conjugated to cyanine-class organic fluorophores through a flexible linker (squiggly line). R represents electronic substituents (*Top*). Schematic shows intramolecular collisions between the triplet state of a fluorophore and the ground state of a COT molecule, facilitating triplet quenching of the fluorophore through TET (*Bottom*). (*C*) Schematics of relative energy changes of a COT molecule in S_0 and T_1 potential energy surfaces (12). ΔE_{inv}, ΔE_{BS}, $\Delta E_{TS(S0)\rightarrow T1vert}$, E_T, and TS are ring inversion barrier energy, bond-shifting energy, energy for vertical excitation from the planar singlet (D_{4h}) to the triplet state, triplet energy, and transition state, respectively. D_{2d}, D_{4h}, and D_{8h} are the Schoenflies point group notations, which collectively represent all symmetry elements within a molecule at a certain structure. While the D_{2d} minimum is puckered, the D_{4h} and D_{8h} transition states are planar and, respectively, bond-length alternate and bond-length equalized forms of COT in the S_0 state. (*D*) Generalized synthetic strategy for self-healing fluorophores. (*E*) Anisotropy of induced current density plot (displayed as clockwise) of an amide substituted COT molecule (AC) in its triplet state (*SI Appendix, Supplementary Methods*). (*F*) Variations of triplet-state ring distortion energies of COT molecules with their triplet energies. Closed circles (green color) refer to COT molecules that were experimentally evaluated. As 1,2-DAC and 1,4-DAC can exist in two bond-shifted isomeric forms, the triplet energy of the most populated form is presented. Optimized triplet-state structures of Me-COT, AC, and DAC are depicted. The bent bow lines indicate steric repulsions. (*G*) Computed triplet energy (E_T) of COT molecules and parent cyanine dyes (*SI Appendix, Supplementary Methods*). Superscript (^{3}) indicates a triplet state.

intensity can fail to increase, and may even reduce, fluorescence emission (16, 17). These considerations put fundamental constraints on the total photon budgets available and hence the speed with which data can be acquired, particularly when the goal is to image fluorescence over extended periods (18, 19).

To extend photon budgets, and to mitigate the impacts of ROS, molecular oxygen can be depleted from solution using enzymatic or degassing procedures (20–23). While such methods can greatly extend the total duration of fluorescence (total photon budget or total time ON), the removal of oxygen, a potent triplet-state quencher (TSQ) (24), tends to reduce fluorophore brightness by increasing the time-averaged duration, and frequency, of triplet and radical states, respectively. The efficiency of molecular oxygen removal can be idiosyncratic (20–23) and can alter physiology and reduce cell viability (25). Photoinduced triplet reactions with the environment are also more prevalent in the absence of oxygen (26, 27). Methods to control the length and duration of triplet excited states are therefore increasingly sought, and efficient strategies to restore the nonemitting, excited-state fluorophore to the ground state have the potential to substantially increase fluorophore brightness, duration, information content, and biological relevance of fluorescence imaging.

The addition of high concentrations (*ca*. 1 mM) of small-molecule TSQs can be used to enhance fluorophore performance (Fig. 1*A*). Such compounds include reducing agents, mixtures of reducing–oxidizing agents (ROXS), protective-agent mixtures, such as cyclooctatetraene (COT), 4-nitrobenzyl alcohol (NBA), and 6-hydroxy-2,5,7,8-tetramethylchroman-2-carboxylic acid (Trolox), or antifade solutions that quench triplet and radical states (9, 28–32). TSQs of this kind generally operate through collision-based mechanisms (31). Despite the value of such methods, the use of solution additives is limited by their relatively low and varied solubilities (31), their propensities to chemically react with excited-state fluorophores (33, 34), and their capacities to perturb biological systems of interest (35). Saturating additive concentrations are also generally ineffective in ambient solution conditions (oxygenated buffers) due to their poor triplet-state quenching efficiency relative to molecular oxygen, which is present in solution at high levels at atmospheric pressure (~0.3 mM) (9).

In order to bypass complications associated with oxygen scavenging and solution additive approaches in biological settings, we developed intramolecular triplet-state quenching strategies in which one or more TSQs are proximally linked to a water-soluble organic fluorophore to increase the effective TSQ concentration (Fig. 1*B*) (36–38). The intramolecular triplet-state quenching, or self-healing (39, 40), strategy dramatically enhances the performance of chemically diverse fluorophores and can be achieved using a variety of TSQ moieties (36–38, 41, 42). Intramolecular chemistries can also compete with unwanted fluorophore reactions with molecular oxygen (36, 43). Advances on this front have led to the development of bright, photostable, and less phototoxic fluorophores spanning the visible spectrum (37, 38). Such tools are particularly advantageous for studies in living cells where physiology may depend on oxygenated environments and the absence of solution additives (36, 38).

Distinct TSQs mediate alternative mechanisms of intramolecular triplet-state quenching (41, 44), including ping-pong redox chemistries and charge separation-independent triplet–triplet energy transfer (T-TET or TET) (39, 40). Redox reactions, while useful, have the tendency to reduce fluorophore brightness by quenching singlet excited states and can be highly sensitive to environment (36, 44–46). By contrast, TET mechanisms are comparatively insensitive to environment and hence hold the promise of enabling a robust and general self-healing approach for a diversity of experimental settings and organic fluorophore species (36–38, 41, 42).

COT is the most effective TSQ thus far identified that is capable of enhancing fluorophore performance via intramolecular TET. COT-mediated TET can improve the performance characteristics of chemically distinct fluorophore species, particularly red-emitting fluorophores with relatively low excited-state reduction potentials (37, 42). To date, the fastest experimentally documented rate of COT-mediated intramolecular TET to an organic fluorophore is on the order of 1×10^6 s^{-1} (38, 41). Principles of intramolecular chemistry and other theoretical considerations suggest, however, that TET rates exceeding 1×10^{10} s^{-1} may be possible (47, 48). Such findings anticipate an opportunity to further enhance organic fluorophore performance across the visible spectrum through a deeper understanding of the COT-mediated self-healing mechanism.

The rate of COT-mediated intramolecular TET can be limited by a number of distinct factors, including intrinsic features of the eight-membered COT ring that govern its capacity to undergo TET as well as features of the fluorophore–TSQ conjugate that determine the likelihood of productive TET collisions (36, 38, 41). COT's ground-state, tub-shaped conformations (D_{2d}) interconvert via planar transition states (D_{4h}) that exchange via bond shift through a D_{8h} transition state (Fig. 1*C*) (12, 49–51). Because planar ground-state COT conformations are on the path to an energetically stabilized, planar Baird aromatic triplet state—which only certain $4n$ π electronic systems can achieve (52, 53)—they are considered essential for TET (Fig. 1*C*). COT's ring inversion energy barrier [ΔE_{inv} of ~42 kJ/mol to 46 kJ/mol (54, 55)] and related D_{8h} transition state [~13 kJ/mol to 17 kJ/mol of additional energy (55)] (ΔE_{BS}; Fig. 1*C*) are thermally accessible on the microseconds time scale at room temperature (56). Structural features that influence ring inversion rates and planar transition-state accessibility are therefore expected to alter TET rates. COT's photochemical stability (57, 58) and Baird aromatic triplet-state lifetime [~0.1 ms (59)] must also be considered in experimental settings that demand continuous illumination. Repetitive intramolecular TET reactions require that triplet-state COT quickly relaxes back to the ground state prior to its own destruction by ROS and its photoreaction with the excited-state fluorophore to which it is linked (38).

In order to maximize the self-healing mechanism in organic fluorophores commonly used in a broad array of imaging applications, we have sought to clarify generalized strategies for modulating the TET rate by physically altering COT's triplet-state energy (E_T; Fig. 1*C*). Cyanine-class fluorophores serve as an ideal starting point for these initiatives, as they are spectrally diverse and widely employed by the medical and fundamental research communities (9, 60). Here, we performed an array of quantitative photophysical investigations of chemically distinct self-healing Cy3, Cy5, and Cy7 fluorophores bearing COT derivatives with specifically tailored triplet energies and charge densities. These pursuits were enabled by appending one or more electron-withdrawing amide substituents to COT and generalizing a synthetic strategy for coupling the amide–COT (AC) derivatives to amine-activated Cy3, Cy5, and Cy7 fluorophores. We also examined the impact of additional charged groups linked to the fluorogenic center, which were employed to improve their performance in biological settings by increasing their aqueous solubility, as well as reducing their aggregation and nonspecific binding propensities (61). These efforts helped establish a mechanistic framework for maximizing the potential of the COT-mediated self-healing mechanism, wherein the triplet energy and lifetime of the COT substituent must be appropriately tuned to match the unique properties and performance features of the fluorophore to which it is attached. They also enabled us to achieve enhancements in the photostability and brightness of self-healing cyanine dyes that exceeded all prior achievements in this area (37, 38) and superior performance metrics compared to other fluorophore classes commonly

employed for single-molecule imaging applications under optimized imaging conditions. Consistent with the observed performance enhancements correlating with reductions in fluorophore triplet-state lifetimes (38, 41), we observed parallel reductions in ROS generation. We leveraged these improvements on the self-healing technology to achieve robust, submillisecond recordings of protein dynamics in ambient oxygen without solution additives using both wide-field total internal reflection fluorescence (TIRF) and confocal based single-molecule Förster (fluorescence) resonance energy transfer (smFRET) techniques (62, 63). These findings extend the potential for imaging single molecules in vitro and in live-cell applications at physiological oxygen concentrations in the kilohertz regime.

Results

Fermi's Golden Rule in the Context of Fluorophore Performance. A single COT molecule covalently attached to the Cy5 fluorophore can notably enhance its photostability (36). However, the same strategy has less impact on other fluorophores in the cyanine class, including only marginal improvements to the performance of Cy3 (37). Both Cy3 and Cy5 covalently linked to COT bearing an amide electron-withdrawing moiety (AC) can exhibit superior photostability relative to the parent COT compounds. For the Cy5 fluorophore, these findings were attributed, in part, to AC mediating faster rates of TET than COT (38). These findings led us to hypothesize that the amide substituent alters COT's intrinsic dynamics or Baird aromatic triplet-state energy in a manner that enhances TET, and thereby fluorophore performance.

According to classical photophysics concepts (64, 65), if intramolecular or intermolecular collisions are physically favorable, the probability of triplet-state energy transfer from one molecule to another—in this case, the fluorogenic center to the intramolecularly linked TSQ—has the tendency to be increased if the process is energetically downhill. Perturbation theory and Fermi's golden rule (66, 67) specifically predict that the TET rate should increase when the energy gap between the triplet excited states of a fluorophore and TSQ is small. In this view, we hypothesized that performance enhancements in individual self-healing organic fluorophores may be optimized by choosing a TSQ whose triplet-state energy is closely matched and energetically downhill with respect to the fluorophore to which it is attached.

In order to experimentally examine these hypotheses in a systematic manner, we established a flexible synthetic approach to examine the impact of specific COT derivatives on cyanine-class fluorophores (Fig. 1*D*). In so doing, we synthesized a matrix of comparable Cy3-, Cy5-, and Cy7-linked methyl–COT (Me-COT), AC, or diamide–COT (DAC) conjugates (*SI Appendix*, Fig. S1*A* and *Supplementary Information for Synthesis*). DAC, which contains two amide substituents, was included in this matrix to further examine the impact of electron withdrawing groups and their steric bulk on the ground- and triplet-states energies of a COT molecule. These compounds were also synthesized with sulfonate groups appended to distinct regions of the fluorophore and the second amide group, including a sulfonate on DAC, to increase aqueous solubility.

With these compounds in hand, we performed bulk photolysis measurements to ascertain the distribution and average rate of single TET events. We further performed an array of both ensemble and single-molecule measurements to evaluate the relationship between TET rates and fluorophore performance in both oxygenated and deoxygenated solution conditions. Single-molecule measurements were performed under continuous wave illumination to probe the performance of self-healing fluorophores in the most commonly employed experimental setting, wherein rapid, repetitive TET cycles between the TSQ and fluorophore are required. Under such conditions, the performance of COT-linked fluorophores is expected to be particularly sensitive to the potential energy surfaces of COT's triplet and singlet states as well as the conformational changes that mediate coupling between the two (Fig. 1*C*) (12, 51).

Amide Substituents Predictably Alter the Triplet-State Energy of COT. We first set out to examine the impacts of ring substituents on COT's nonplanar tub-shaped ground-state and planar triplet-state conformations using density functional theory-based quantum chemical calculations (*SI Appendix*, Table S1 and *Supplementary Methods*) (68). The computed energy of the highest-occupied molecular orbital of a ground-state COT molecule decreased with the addition of electron-withdrawing amide substituents. NMR experiments confirmed that amide substituents deshield the ring protons of COT (*SI Appendix*, Fig. S2*A*). This impact, and the hydrophilic nature of the amide group, also increased the aqueous solubility of AC- and DAC-linked fluorophores over COT-linked dyes (*SI Appendix*, Fig. S2*B*) spanning the visible spectrum (*SI Appendix*, Fig. S2 *B–D*). We infer from these observations that the amide substituent's electron-withdrawing capacity modifies physical aspects of COT's ground state.

Analogous quantum mechanical simulations suggested that amide substituents tend to increase the activation energy for ring inversion of the ground-state COT molecule (ΔE_{inv}; Fig. 1*C* and *SI Appendix*, Table S1). These impacts were attributed to increased steric constraints on the eight-membered COT ring (D_{4h}; Fig. 1*C*), as evidenced by the decreased energy for vertical excitation from the planar singlet (D_{4h}) to the triplet state ($\Delta E_{TS(S0)\rightarrow T1vert}$; Fig. 1*C* and *SI Appendix*, Table S1). While the TET mechanism specifies that the true COT ring inversion energies remain on the order of microseconds to be consistent with the experimentally measured TET rates (*ca.* $10^6\ s^{-1}$) (38, 41), the observed trends suggest that amide substituents have a tendency to reduce the ring inversion rates of the COT molecule (*SI Appendix*, Fig. S3*A*) as well as the time-averaged occupancies of planar transition states (D_{4h} and D_{8h}). Although absolute values cannot be determined from the calculations performed, the trends predict reduced planarization rates and reductions in COT-mediated TET rates. Paradoxically, however, the effect of increasing COT's triplet-state energy (E_T; Fig. 1*C*) in the energy gap framework is to close the gap with the fluorophore's triplet energy, thereby increasing the TET rate. These considerations collectively suggest that ring substituents can impact COT's TET properties via multiple mechanisms that are counterposing, in which the energy of the triplet state plays a central role.

Quantum chemical calculations on chemically diverse COT derivatives further revealed that both the size and number of substituents on COT's ring structure can tune its triplet-state energy (E_T) (*SI Appendix*, Table S1). Here, we observed that DAC, which has two amide substituents, exhibited higher triplet-state energy than both AC and COT. The calculations on Me-COT, AC, and DAC specifically revealed that each compound retains diatropic currents within the planar COT ring in the triplet state, as well as other aromatic indicators that define Baird aromaticity (Fig. 1*E* and *SI Appendix*, Fig. S3 *B* and *C*). The Baird aromatic features of Me-COT, AC, and DAC provide enhanced triplet photostability as evidenced from the computed Gibbs energies of reaction with molecular oxygen, which were found to be endergonic for COT molecules but exergonic for regular singlet-state Hückel aromatic TSQs (*SI Appendix*, Table S2). Steric congestion between the amide groups and neighboring hydrogen atoms in the conjugated π-ring increased triplet-state ring distortion energy (Fig. 1 *F*, *y* axis; *SI Appendix*, Fig. S3*D*, *x* axes; and *SI Appendix*, Table S1), which positively correlated with triplet-state energies (Fig. 1 *F*, dashed line). We conclude from these observations that amide substituents increase the energies of near-planar or planar COT transition states and sterically destabilize the triplet state. These impacts are expected to reduce the energy gap with relatively high-energy

triplet-state fluorophores so as to promote TET and to facilitate formation of COT's Baird aromatic triplet state.

Fermi's Golden Rule Is Predictive of Fluorophore Performance. Given the computed triplet-state energy values of COT molecules and parent cyanine fluorophores (Fig. 1*G* and *SI Appendix*, Table S1), we set out to examine the utility of the energy gap framework for predicting fluorophore performance. To examine fluorophore performance, we employed ensemble, single-turnover TET measurements using laser flash photolysis (LFP) and single-molecule measurements that enforce multiturnover TET conditions. We began by taking LFP measurements of the triplet-state lifetimes (τ_T) of Me-COT–, AC-, and DAC-linked Cy3, Cy5, and Cy7 fluorophores to establish their single-turnover, instantaneous TET rate constants ($1/\tau_T$) (Fig. 2 *A*, *x* axes; *SI Appendix*, Table S3 and *Supplementary Methods*). To increase the robustness of submicrosecond TET measurements, we employed an intramolecular photosensitization approach in which the triplet state sensitizer "OTX" (9-oxothioxanthene) is covalently attached to each molecule (38) (*SI Appendix*, Fig. S4 *A–D*). Globally consistent with the anticipated mechanistic framework, as well as previous measurements (38), we found that both Me-COT and AC efficiently quenched the triplet states of Cy5 and Cy7. By contrast, Me-COT and AC were relatively inefficient for the Cy3 fluorophore, particularly in the case of Me-COT, which exhibits a larger relative energy gap with the Cy3 triplet state.

We next examined the impact of the fluorophore structural changes due to the additional hydrophilic sulfonate substituents on each of the cyanine indole rings (two versus four sulfonates total; 2S vs. 4S). The additional sulfonates increased the fluorescence lifetimes and quantum yields of Cy3-AC and Cy5-AC (*SI Appendix*, Table S3, Fig. S5, and *Supplementary Methods*). These impacts generally paralleled reduced rates of nonradiative processes from the singlet excited state (S_1) but showed contrasting effects on TET rates (Fig. 2*A*, *x* axes). These observations indicate that TET rates may also be influenced by modifications of physical features of the fluorophore, which may include impacts on the rate of intersystem crossing, the likelihood of physical interactions with the covalently attached TSQ, and solvent organization around ground and excited states. Unexpectedly, the observed TET rates were slower for Cy3-4S-DAC and Cy5-4S-DAC derivatives compared to AC. We attribute these findings to the aforementioned complexities, including effects related to the additional charge substituent on the DAC molecule and the reduced time-averaged occupancy of DAC in its near-planar transition states (Fig. 1*C* and *SI Appendix*, Fig. S3*A* and Table S1). We conclude from these findings that, although the energy gap framework provides advantageous predictive power, additional variables influencing experimental performances under multiturnover conditions must also be considered.

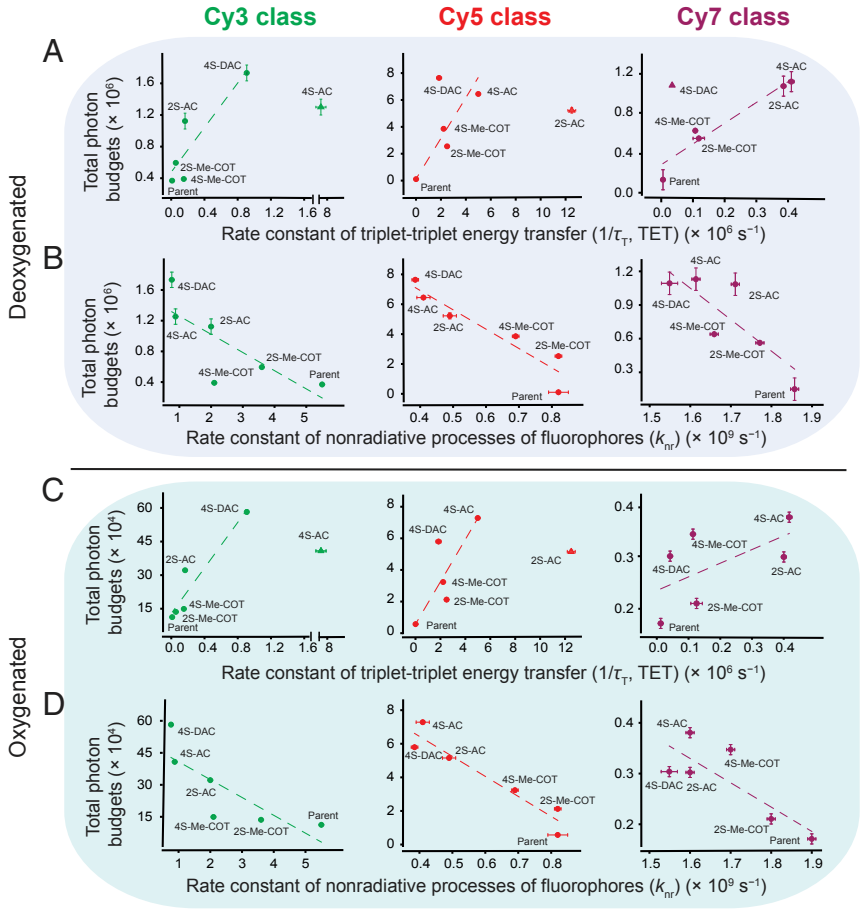

Fig. 2. Correlations of fluorophore photostability with TET rate as well as nonradiative processes of fluorophores. Correlations of single-molecule total photon budgets of cyanine dyes bound to DNA oligonucleotides in (*A*) deoxygenated and (*C*) oxygenated imaging buffers with rate constants of TET ($1/\tau_T$). Correlations of the single-molecule total photon budgets in (*B*) deoxygenated and (*D*) oxygenated imaging buffers with rate constants of nonradiative processes (k_{nr}) from singlet excited state (S_1) of the fluorophores. Single-data point outliers in each data set were not included in the correlations (see *Results*). The single-molecule data were an average of six movies from at least two independent experiments (*SI Appendix*, *Supplementary Methods*). Error bars are SDs.

To evaluate fluorophore performance under multiturnover TET conditions, we measured the total number of photons emitted by each fluorophore bound to a DNA oligonucleotide prior to photobleaching (total photon budget) using continuous wave illumination, single-molecule TIRF microscopy (*SI Appendix*, *Supplementary Methods*) (69). Here, we observed positive correlations between the enhancements in total photon budgets and the TET rates for all three classes of dyes (Cy3, Cy5, and Cy7) in deoxygenated (Fig. 2*A*, dashed lines) as well as oxygenated (Fig. 2*C*, dashed lines) conditions. The total photon budgets were also inversely correlated with nonradiative processes, including cis–trans isomerization rates (Fig. 2 *B* and *D*, dashed lines). These data are consistent with a maximization of cyanine fluorophore performance when nonfluorescent decay pathways are minimized. These findings are also in line with ROS being the primary pathway by which fluorophore photobleaching occurs (9).

Photobleaching rates for Cy3, Cy5, and Cy7 parent dyes followed the order Cy3 < Cy5 < Cy7, consistent with triplet energy gaps of each fluorophore with respect to molecular oxygen (singlet oxygen energy is 94 kJ/mol) (65). As expected from the reduction in the triplet-state lifetimes evidenced for Me-COT–, AC-, and DAC-linked fluorophore derivatives (*SI Appendix*, Table S3), we observed both enhanced bulk photostability and marked reductions in the ROS generation rates in oxygenated environments (*SI Appendix*, Fig. S6 *A–E* and *Supplementary Methods*). Reducing environments ensure the stability of biological samples, including the oxygen scavenging systems employed to stabilize fluorescence (9). While low concentrations of β-mercaptoethanol (BME) specifically reduced the photostability of the parent Cy5, the photostabilities of self-healing Cy3, Cy5, and Cy7 fluorophores were largely unaffected (*SI Appendix*, Fig. S7 *A* and *B* and *Supplementary Methods*). These observations are consistent with BME covalently reacting with the polymethine chain in parent cyanine fluorophores to interrupt fluorescence (33, 34), and that such reactions are mitigated by the shortened triplet-state lifetimes of self-healing fluorophores.

The self-healing Cy3, Cy5, and Cy7 derivatives examined exhibited up to 5-, 76-, and 7-fold enhancements in photostability in deoxygenated conditions compared to their parent fluorophore counterparts (Fig. 2 *A*, *y* axes; *SI Appendix*, Table S3 and Movies S1–S3). In oxygenated conditions, Cy3, Cy5, and Cy7 derivatives exhibited 5-, 13-, and 2-fold enhancements in photostability compared to respective parent dyes (Fig. 2 *C*, *y* axes; *SI Appendix*, Table S3 and Movies S4–S6). These photostabilities are notably improved relative to preexisting self-healing dyes (38). In deoxygenated solutions under relatively standard illumination regimes (~8 KHz photon count rate), the observed increases in brightness and durability of Cy3-4S-DAC and Cy5-4S-DAC (or Cy5-4S-AC) compared to Cy3-2S-AC and Cy5-2S-AC equated to roughly 0.5 million and 1 million to 2 million photon increases in total photon budget, respectively (Fig. 2 *A*, *y* axes; *SI Appendix*, Table S3). Significant enhancements in Cy3-4S-DAC and Cy5-4S-AC performance were also observed in oxygenated solutions (Fig. 2 *C*, *y* axes; *SI Appendix*, Table S3). Notably, the observed increases in total photon budgets showed positive correlations with the calculated triplet-state ring distortion energies of the COT molecules (*SI Appendix*, Fig. S3*D*). This finding is consistent with the notion that AC and DAC derivatives exhibit shortened triplet lifetimes compared to Me-COT because of increased strain on planar configurations of the COT ring (Fig. 1*F*). These data suggest that COT molecules with

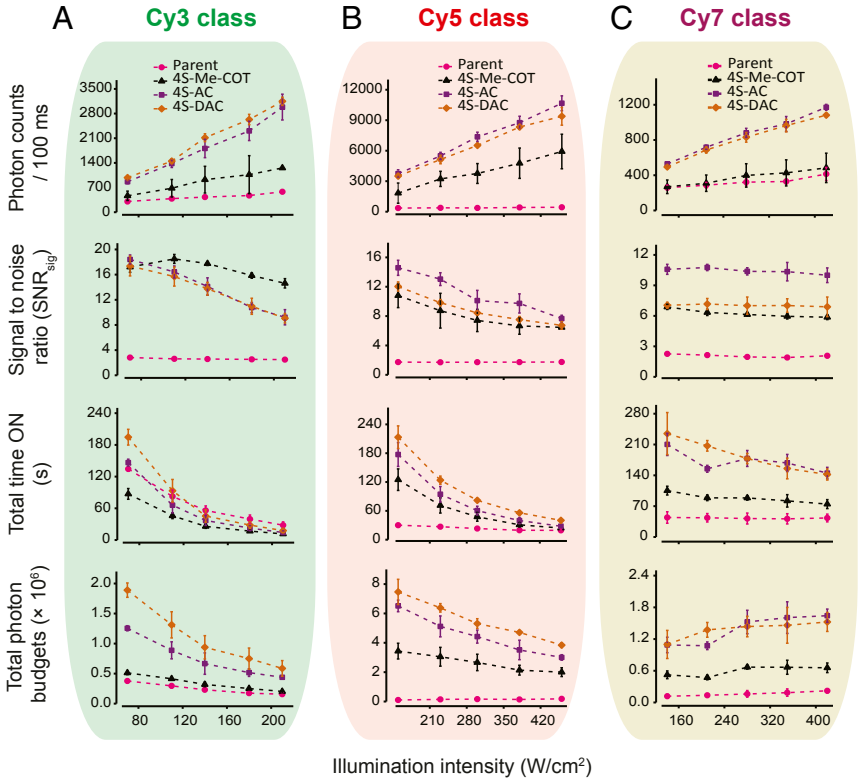

Fig. 3. Improved performance of self-healing fluorophores at high illumination intensities. Illumination intensity-dependent photon counts (brightness; *Top*), signal to noise ratio (SNR$_{sig}$, a measure of the variance of fluorescence signal over time; *Upper Middle*), total time ON (total survival time prior to photobleaching; *Lower Middle*), and total photon budgets (total number of photons emitted prior to photobleaching; *Bottom*) of (*A*) Cy3, (*B*) Cy5, and (*C*) Cy7 class of fluorophores bound to DNA oligonucleotides in deoxygenated imaging buffers. The single-molecule data were an average of three movies from three independent experiments. The error bars are SDs.

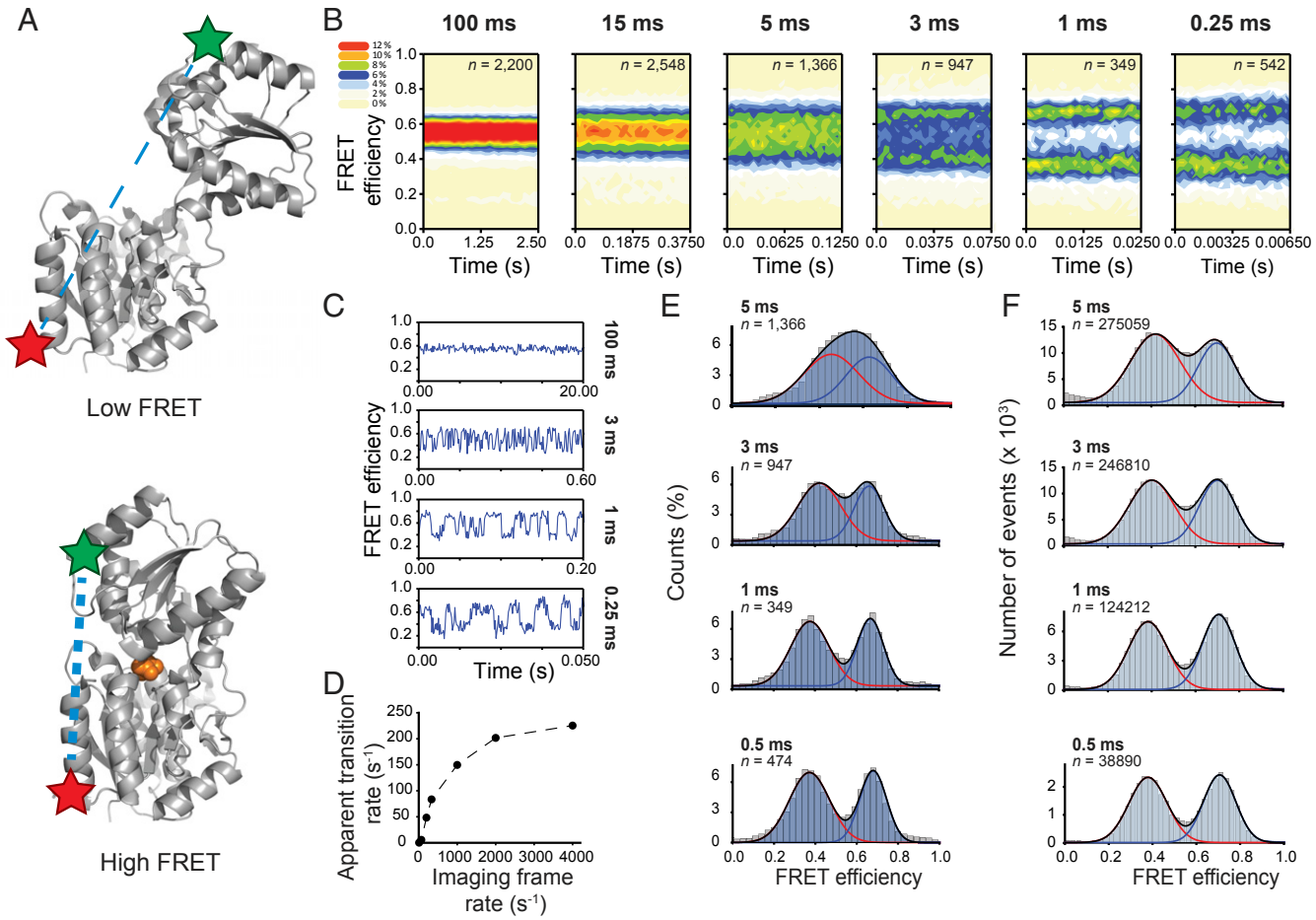

Fig. 4. Submillisecond protein dynamics in the presence of ambient oxygen. (*A*) Crystal structures of open (*Top*) (RCSB Protein Data Bank [PDB] ID code 1Z15) and leucine (orange)-bound closed (*Bottom*) (PDB 1Z16) forms of LIV-BP^{SS}. Star symbols indicate labeling sites of the donor and acceptor fluorophores to LIV-BP^{SS}. Low and high FRET efficiency populations correspond to LivJ unbound and bound to Leucine, respectively. (*B*) Population FRET contour plots of surface immobilized LIV-BP^{SS} labeled with Cy3-4S-DAC and Cy5-4S-AC in the presence of 4.5 μM leucine, recorded in a TIRF setup (*SI Appendix, Supplementary Methods*), color coded to reflect the relative population of the imaged molecules. (% given in the color coded legend). *n* indicates number of single molecules. (*C*) Representative smFRET trajectories of the surface immobilized LIV-BP^{SS} at 100-ms (*Top*), 3-ms (*Upper Middle*), 1-ms (*Lower Middle*), and 0.25-ms (*Bottom*) time resolutions. (*D*) Variation of the apparent transition rate of the surface immobilized LIV-BP^{SS} between unbound and bound conformations with imaging frame rate. Apparent transition rates were calculated as the total number of observed transitions between nonzero FRET states divided by the total time in these states across all traces. (*E*) Cumulative population histograms of the surface immobilized LIV-BP^{SS} at 5-, 3-, 1-, and 0.5-ms time resolutions. (*F*) FRET efficiency histograms (5-, 3-, 1-, and 0.5-ms binning) of freely diffusing LIV-BP^{SS} labeled with Cy3-4S-DAC and Cy5-4S-AC dyes in the presence of 5 μM leucine, recorded in a confocal TCSPC setup. At the protein concentration used for these experiments, there is an 82% and 88% probability [p_{same} (80); *SI Appendix, Supplementary Methods*] that fluorescence bursts are emitted by the same protein molecule after 5 and 3 ms, respectively.

relatively short-lived triplet states are particularly advantageous to fluorophore performance under continuous illumination where fluorophores repetitively enter triplet states and thus require multiple TET events.

Self-Healing Cyanine-Class Fluorophores Exhibit Unusually High Intrinsic Brightness. High illumination intensities are essential for achieving time resolutions and signal-to-noise ratios sufficient to capture fast molecular processes. Standard cyanine and rhodamine fluorophores generally show poor performance in this regime, as triplet and radical states become increasingly populated (70). In the absence of protective strategies, this can limit single-molecule imaging studies to illumination regimes of ∼5 kHz to 10 kHz and time resolutions of 10 to 100 frames per s (10- to 100-ms integration times), equating to ∼10 photons per ms to 50 photons per ms. In line with this notion and efficient, multiturnover triplet-state quenching in self-healing dyes, each of the fluorophore–COT conjugates showed marked increases in brightness (photon count rates) at increasing illumination intensities, while the brightness of each parent fluorophore remained nearly constant. At the highest illumination intensity investigated (Fig. 3, last point on *x* axes), Cy3-4S-DAC, Cy5-4S-AC, and Cy7-4S-AC derivatives exhibited 5-, 25-, and 3-fold greater brightness, respectively, than their parent fluorophores (Fig. 3 *A*–*C*, *Top*) in deoxygenated solutions in the absence of solution additives. At high time resolution (1 ms), Cy3-4S-DAC and Cy5-4S-AC yielded ∼1,000 photons per ms to 1,500 photons per ms, which outcompeted both Cy3B and ATTO 647N, widely considered the brightest organic dyes available (7)—even when interrogated in the presence of solution additives (*SI Appendix*, Fig. S8).

The total photon budgets for all fluorophore derivatives examined were notably higher over a threefold range of illumination intensities compared to their parent fluorophore counterparts (Fig. 3 *A*–*C*). At the lowest power examined (Fig. 3, *x* axes), the total photon budgets were 5-, 62-, and 9-fold higher for Cy3-4S-DAC, Cy5-4S-AC, and Cy7-4S-AC, respectively, and, at 3 times the power (Fig. 3, *x* axes), 4-, 16-, and 7-fold higher, respectively. Under all conditions, the signal-to-noise ratio (SNR_{sig}), a metric

quantifying the intensity and variance of the fluorescence signal, remained at least fourfold higher than the parent compounds. The difference in the total duration of fluorescence (total time ON) between self-healing and parent fluorophores was observed to diminish at increased illumination intensity. This trend was steepest for Cy3 fluorophore derivatives (Fig. 3 *A*, *Lower Middle*), perhaps indicative of the negative impacts of photoisomerization, which are exacerbated for shorter polymethine chain lengths (Fig. 2*B*, nonradiative rates in *x* axes) (60). The observed reductions in fluorophore performance at higher illumination intensities could, however, also arise from a number of additional considerations, including power-dependent increases in the saturation of fluorophore triplet states, the negative contributions of higher-order excited states, and the finite rates of TSQ relaxation from triplet states.

Self-Healing Fluorophores Exhibit Superior Performance against Known Benchmarks. Under multiturnover illumination conditions, the best-performing self-healing cyanine dyes (Cy3-4S-DAC, Cy5-4S-AC, and Cy7-4S-AC) consistently outperformed parent dyes even when solution-based intermolecular quenching strategies were employed, particularly in the presence of oxygen (*SI Appendix*, Fig. S9) (36). Each fluorophore also exhibited significantly reduced blinking rates and durations (*SI Appendix*, Fig. S10). The best-performing self-healing cyanine dyes outperformed other commonly employed, commercially available, rhodamine and cyanine class of fluorophores (*SI Appendix*, Fig. S1*B*) in both oxygenated and deoxygenated imaging environments (*SI Appendix*, Fig. S11), even in the presence of solution additives (*SI Appendix*, Fig. S12). Although ATTO 647N was capable of outcompeting Cy5-4S-AC in the presence of oxygen in terms of total time ON at low illumination intensities (*SI Appendix*, Fig. S12*B* and *Supplementary Methods*), the use of ATTO 647N presents significant drawbacks in practical experimental settings, including ROS generation (43), nonspecific binding (71), and idiosyncratic deviations in photon flux (7, 72) (*SI Appendix*, Fig. S13).

Submillisecond Protein Dynamics in the Presence of Oxygen. Wide-field, camera-based fluorescence imaging methods can be used to quantify large-scale conformational dynamics related to function within an ensemble (hundreds to thousands) of individual, surface-immobilized biomolecules simultaneously (69). As discussed above, and elsewhere (18), the temporal resolution of this approach is, however, typically limited to the millisecond regime. By contrast, the quantifications of conformational dynamics using confocal methods, while potentially affording much higher time resolutions than camera-based methods (73–75), are restricted to the analysis of one molecule at a time and typically require highly concentrated photoprotective additives (76, 77).

To examine the potential utility of the best-performing self-healing fluorophores generated in the present study, we set out to perform both confocal and camera-based smFRET investigations in the absence of solution TSQ additives or oxygen scavenging across a range of time resolutions (Fig. 4 and *SI Appendix*, Fig. S14 and *Supplementary Methods*). In these experiments, we

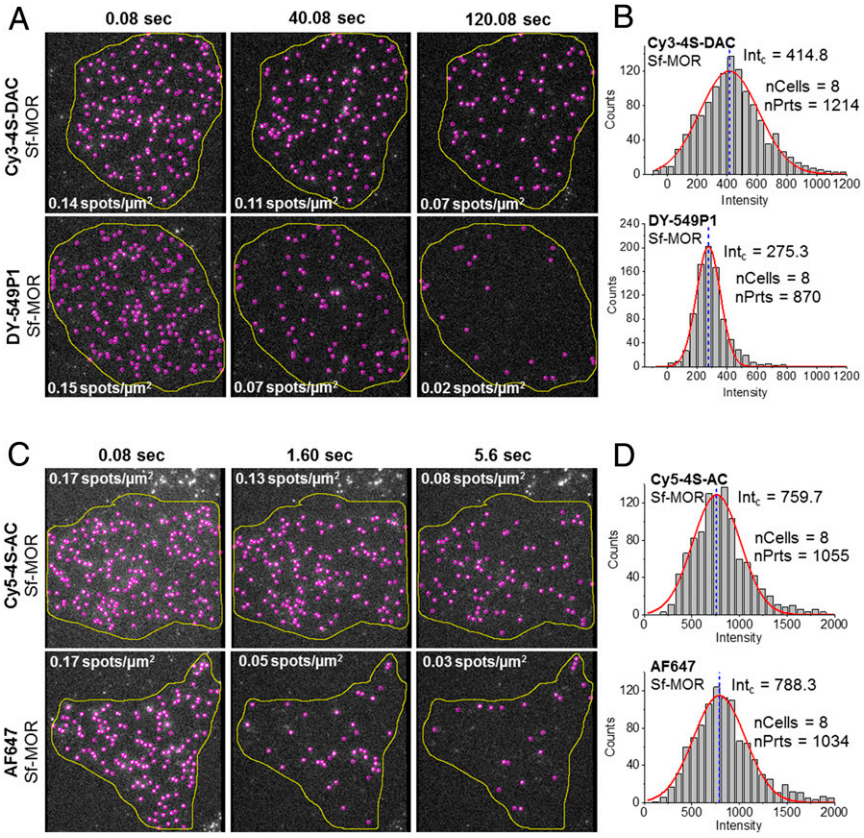

Fig. 5. Live-cell imaging of individual mu opioid receptors at physiological oxygen conditions. Single-molecule TIRF image sequences of CHO cells expressing SNAPf-MOR (Sf-MOR) labeled with (*A*) Cy3-4S-DAC (*Top*) compared with DY-549P1 (*Bottom*) and (*C*) Cy5-4S-AC (*Top*) compared with AF647 (*Bottom*). Detected particles are indicated by purple circles within the cell (region of interest shown in yellow), captured using a 100× objective and an Evolve 512 EMCCD (*SI Appendix, Supplementary Methods*). Fluorescence intensity distributions of SNAPf-MOR labeled with (*B*) Cy3-4S-DAC (*Top*) compared with DY-549P1 (*Bottom*) and (*D*) Cy5-4S-AC (*Top*) compared with AF647 (*Bottom*). Each distribution includes the number of particles (nPrts) from eight different cells (nCells). Solid red line represesnts a Gausssian fit of the data; blue dashed line represents the mean fluorescence intensity (photons/40 ms frame).

employed a periplasmic amino acid binding protein from *Escherichia coli* encoded by the *livJ* gene (78), site-specifically labeled with Cy3-4S-DAC and Cy5-4S-AC on its opposing clam-shell domains (LIV-BP^{SS}; Fig. 4*A* and *SI Appendix*, *Supplementary Methods*), which exhibits both low- (apo) and high- (ligand bound) FRET efficiency states (79). By employing wide-field single-molecule imaging at the K_D of leucine binding (4.5 μM) (79), ligand-binding dynamics could be robustly captured when the time resolution was increased below 5 ms (Fig. 4 *B*, *C*, and *E*). Analogously prepared LIV-BP^{SS} labeled with the parent Cy3/Cy5 fluorophore pair or the Cy3B/ATTO647N fluorophore pair showed relatively poor performance compared to the self-healing fluorophore pair (*SI Appendix*, Fig. S15).

At a time resolution of 250 μs, individual LIV-BP^{SS} molecules labeled with Cy3-4S-DAC and Cy5-4S-AC exhibited an average total photon count rate of ∼500 photons per ms (*SI Appendix*, Fig. S14*B*), enabling the robust quantification of rapid, large-scale conformational dynamics (Fig. 4 *C*, *Bottom*). Using hidden Markov modeling (HMM) methods (69), we found that LIV-BP^{SS} opening and closing cycles increased in parallel with the imaging speed. At imaging speeds greater than ˜2,400 frames per s, the observed dynamics plateaued at a rate of ∼240 s^{-1} (Fig. 4*D* and *SI Appendix*, *Supplementary Methods*). These findings are consistent with previous investigations (81) showing that rates are most accurately estimated using HMM methods when the imaging rate is roughly 10 times faster than the observed conformational process. The enhanced brightness, photostability, and SNR_{sig} of the self-healing fluorophore pair enabled the capture of LIV-BP^{SS} dynamics at time resolutions as high as 100 μs (*SI Appendix*, Fig. S14*C*), an imaging speed that is near the theoretical limit of the approach (18). These findings demonstrate that scientific complementary metal oxide semiconductor detector technologies (69), when used in combination with self-healing fluorophores, can extend the range of time scales that can be imaged and accurately quantified using camera-based methods by up to 50-fold such that the rates of functionally relevant conformational processes are in the kilohertz regime.

Conformational dynamics within LIV-BP^{SS} labeled with Cy3-4S-DAC and Cy5-4S-AC could also be readily evidenced using confocal illumination strategies and time-correlated single-photon counting methods, combined with pulsed interleaved excitation (Fig. 4*F*). Paralleling our camera-based imaging results, FRET efficiency distributions progressively broadened as the binning time approached the interconversion time between unbound and bound states of LIV-BP^{SS} (∼3 ms) (Fig. 4 *E* and *F* and *SI Appendix*, *Supplementary Methods*) (82). While time bins of >1 ms exceeded the average bursts duration of individual molecules, the sample concentration was sufficiently low to allow this semiquantitative analysis (*SI Appendix*, *Supplementary Methods*) (80). These data revealed a global agreement between wide-field and confocal imaging strategies, consistent with the capacity to robustly detect submillisecond conformational dynamics using either approach.

Live-Cell Imaging of Integral Membrane Protein at Physiological Oxygen Concentration. To establish the utility of Cy3-4S-DAC and Cy5-4S-AC for imaging single molecules in living cells at physiological oxygen concentrations, we compared their performance to the cyanine fluorophore derivatives DY-549P1 and AF647 (Alexa Fluor 647) commonly employed for such applications. DY-549P1 and AF647 are in the same chemical class as Cy3 and Cy5 fluorophores (83), but include four sulfonate groups to minimize nonspecific binding to cellular membranes. Correspondingly, we consider them the most appropriate control for self-healing cyanine dyes in this context. Solution-based photoprotecting agents were excluded in this setting due to evidence of significant levels of additive-induced cytotoxicities (*SI Appendix*, Fig. S16 and *Supplementary Methods*). Comparisons with ATTO 647N were not possible due to high nonspecific binding (*SI Appendix*, Fig. S17 *A* and *B*) (83).

We performed objective-based single-molecule TIRF imaging experiments on Chinese Hamster ovary (CHO) cells stably expressing human mu opioid receptors amino-terminally tagged with a SNAPfast moiety (SNAPf-MOR) labeled with either benzylguanine-activated Cy3-4S-DAC, DY-549P1, Cy5-4S-AC, or AF647 (*SI Appendix*, *Supplementary Methods*). In this context, both Cy3-4S-DAC and Cy5-4S-AC exhibited ∼threefold to fourfold longer duration of fluorescence (total time ON) compared to DY-549P1 and AF647, respectively, as well as additional enhancements in overall brightness (Fig. 5 and *SI Appendix*, Fig. S17 *C* and *D*). These global improvements in performance should enable the acquisition of robust longer-lived single-particle tracking data in ambient oxygen environments suitable for living cells.

Discussion

Since the introduction of the self-healing strategies for improving the performance of organic fluorophores in biological settings

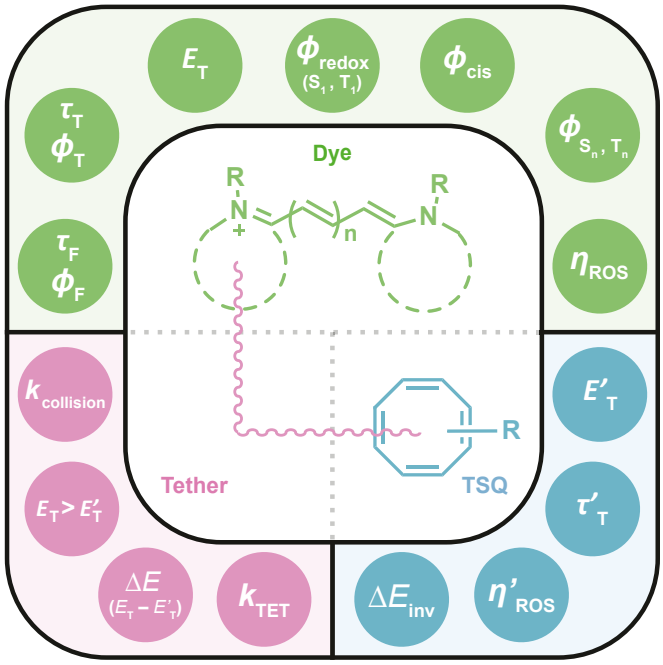

Fig. 6. Schematic summary of important photophysical, photochemical, and thermodynamical parameters of a fluorophore and a COT molecule that together govern the performance of a self-healing fluorophore. Although interrelated, green circles are depicted as corresponding to fluorophore (generic cyanine structure; top quadrant) parameters; blue circles as TSQ (COT; lower right quadrant) parameters; and pink circles are tether (linker; lower left quadrant) parameters that require considerations of both fluorophore and TSQ. R represents electronic substituents. τ_F and ϕ_F are fluorescence lifetime and fluorescence quantum yield of a fluorophore, respectively. τ_T, ϕ_T, and E_T are lifetime, quantum yield, and energy of a triplet-state fluorophore, respectively. $\phi_{redox\ (S1,\ T1)}$, ϕ_{cis}, and $\phi_{(Sn,\ Tn)}$ are quantum yields of redox species from both singlet (S_1) and triplet (T_1) states, quantum yields of cis-isomer state, and quantum yields of higher-order singlet (S_n) and triplet (T_n) excited states of a fluorophore, respectively. ΔE_{inv} is the ring inversion barrier energy of a COT molecule in its singlet ground state (S_0). τ'_T and E'_T are lifetime and energy, respectively, of a triplet-state COT molecule. η_{ROS} and η'_{ROS} refer to chemical reactivity of a fluorophore and a COT molecule with ROS, respectively. ΔE ($E_T - E'_T$) is the triplet–triplet energy difference of a fluorophore and a COT molecule; $k_{collision}$ is the rate constant of intramolecular collisions between a triplet-state fluorophore and a singlet ground-state COT molecule; k_{TET} is the TET rate constant from a triplet-state fluorophore to a COT molecule.

(36, 37), a principle goal has been to harness this approach to reliably and predictably enhance distinct organic fluorophore species to capture their full performance potential. Here, we show that tailored modifications to COT's triplet-state energy and lifetime increase the performance characteristics of Cy3, Cy5, and Cy7, including their brightness, photostability, and regularity of photon flux, parameters reflected in the experimental SNR_{sig}. The best-performing organic fluorophore species generated through the present investigations extend the time resolution of both wide-field and confocal fluorescence microscopy investigations of biological systems to the kilohertz regime in the absence of oxygen scavenging and potentially toxic solution additives. The enhanced TET rates also markedly reduced ROS generation, consistent with the altered COT derivatives more effectively competing with undesirable reactions with molecular oxygen.

Our findings further suggest that COT's propensity to achieve a relatively photostable, Baird aromatic triplet state contributes to its robustness as an agent for intramolecular TET. They also show that COT's triplet-state energy can be predictably tuned by sterics to reduce the energy gap between it and the triplet-state energies of the fluorophore to which it is attached. By contrast, compounds with regular triplet states, which are aromatic in the ground state (e.g., substituted benzenes, naphthalene, anthracene, and rubrene) (65), are rendered ineffective in this capacity because they can absorb and fluoresce in the visible spectrum, and their triplet states can be quenched by molecular oxygen at rates that are two orders of magnitude higher than COT (59).

The correlations between COT's triplet-state energy, TET rates, and fluorophore performance reported herein provide compelling experimental evidence that the self-healing mechanism—and COT's effectiveness in this context—mirror perturbation theory and Fermi's golden rule (66, 67). This framework specifies that the intramolecularly linked TSQ undergoes the most efficient and rapid TET when its triplet-state energy is closely matched, and lower than that of the fluorophore, so that TET is both spontaneous and kinetically favorable. In its generalizable form, this framework can be applied to adopt more effective self-healing strategies for a diverse range of fluorophores and fluorescence applications, including routine ensemble fluorescence investigations where molecular oxygen is present, as well as live-cell imaging applications. The presented investigations lead us to conclude, however, that multiple parameters, in addition to Fermi's golden rule, must also be considered to further enhance fluorophore performance in experimental settings. In this regard, particular attention should be given to complete evaluations of the photophysical, photochemical, and thermodynamic parameters of the organic fluorophore species under consideration, the TSQ employed, and the molecular tether linking these two species (Fig. 6). Salient variables include the intrinsic redox potentials of organic fluorophores, the tether composition and tethering geometry, and the intrinsic properties of the TSQ, including consideration of its performance in multiturnover TET settings, where it must repetitively relax from triplet excited states prior to reaction with the surrounding environment and molecular oxygen (Fig. 6). The importance of such considerations is highlighted by recent investigations showing that the photobleaching of self-healing organic fluorophores may occur by way of TSQ destruction (38) and evidence that the burdens of multiturnover TET can be partially alleviated by covalent linkage of more than one TSQ to the fluorogenic center (38). We expect the theoretical and experimental strategies presented will inform, and thereby increase speed and efficiency, of such initiatives, including endeavors to more effectively extend the self-healing strategy to rhodamine-class fluorophores commonly employed for intracellular imaging applications (38, 84–86).

Additional optimizations of the self-healing mechanism will benefit from the implementation of new COT derivatives that exhibit even faster TET rates and further evaluation of COT-derivative performance under multiturnover conditions and high illumination intensities. Efforts of this kind will be particularly enabled by further investigations into how to increase the ring inversion rates of ground-state COT molecules and to modify the triplet lifetimes of COT derivatives in predictable fashions (Fig. 6). Quantum chemical calculations may be advantageous in this regard. The identification of chemically distinct species that exhibit Baird aromatic triplet states, which can be predictably tuned for optimal experimental performances, will also be of great advantage. New TSQs of this kind will add additional information about the self-healing mechanism. They will also expand the universe of self-healing organic fluorophores to enable more robust, and even unforeseen, biological research initiatives.

Methods

Fluorophore Synthesis and Ensemble and Single-Molecule Experiments. Cy3, Cy5, and Cy7 classes of self-healing dyes depicted in *SI Appendix*, Fig. S1*A* were synthesized in-house, and their syntheses are described in *SI Appendix, Supplementary Information for Synthesis*. The rhodamine and cyanine class of fluorophores depicted in *SI Appendix*, Fig. S1*B* were purchased from various commercial sources. All ensemble and single-molecule experimental procedures are described in *SI Appendix, Supplementary Methods*.

Data Availability. All experimental data, materials, and software are available upon request.

ACKNOWLEDGMENTS. This work was supported by the NIH (Grant R01GM098859 to S.C.B., and Grant R01MH54137 to J.A.J.). We are grateful to the Wenner-Gren Foundations for a postdoctoral fellowship to O.E.B. We thank Dr. Sukanta Bar and the Chemical Biology and Therapeutics Department at St. Jude Children's Research Hospital (SJCRH) for providing feedback on supplementary information for synthesis, and we thank Emily J. Rundlet for graphical expertise. We also acknowledge and thank Dr. Ravi Kalathur and the Protein Technologies Center, the Single-Molecule Imaging Center, and the Cell & Tissue Imaging Center (Program NCI P30 CA021765), which receive support from SJCRH.

1. W. E. Moerner, Y. Shechtman, Q. Wang, Single-molecule spectroscopy and imaging over the decades. *Faraday Discuss.* **184**, 9–36 (2015).
2. S. W. Hell *et al*., The 2015 super-resolution microscopy roadmap. *J. Phys. D Appl. Phys.* **48**, 443001 (2015).
3. Z. Liu, L. D. Lavis, E. Betzig, Imaging live-cell dynamics and structure at the single-molecule level. *Mol. Cell* **58**, 644–659 (2015).
4. S. J. Sahl, S. W. Hell, S. Jakobs, Fluorescence nanoscopy in cell biology. *Nat. Rev. Mol. Cell Biol.* **18**, 685–701 (2017).
5. Y. M. Sigal, R. Zhou, X. Zhuang, Visualizing and discovering cellular structures with super-resolution microscopy. *Science* **361**, 880–887 (2018).
6. G. T. Dempsey, J. C. Vaughan, K. H. Chen, M. Bates, X. Zhuang, Evaluation of fluorophores for optimal performance in localization-based super-resolution imaging. *Nat. Methods* **8**, 1027–1036 (2011).
7. T. Ha, P. Tinnefeld, Photophysics of fluorescent probes for single-molecule biophysics and super-resolution imaging. *Annu. Rev. Phys. Chem.* **63**, 595–617 (2012).
8. E. M. S. Stennett, M. A. Ciuba, M. Levitus, Photophysical processes in single molecule organic fluorescent probes. *Chem. Soc. Rev.* **43**, 1057–1075 (2014).
9. Q. Zheng *et al*., Ultra-stable organic fluorophores for single-molecule research. *Chem. Soc. Rev.* **43**, 1044–1056 (2014).
10. B. Kozankiewicz, M. Orrit, Single-molecule photophysics, from cryogenic to ambient conditions. *Chem. Soc. Rev.* **43**, 1029–1043 (2014).
11. G. Gut, M. D. Herrmann, L. Pelkmans, Multiplexed protein maps link subcellular organization to cellular states. *Science* **361**, eaar7042 (2018).
12. P. G. Wenthold, D. A. Hrovat, W. T. Borden, W. C. Lineberger, Transition-state spectroscopy of cyclooctatetraene. *Science* **272**, 1456–1459 (1996).
13. A. Gust *et al*., A starting point for fluorescence-based single-molecule measurements in biomolecular research. *Molecules* **19**, 15824–15865 (2014).
14. R. Menzel, E. Thiel, Intersystem crossing rate constants of rhodamine dyes: Influence of the amino-group substitution. *Chem. Phys. Lett.* **291**, 237–243 (1998).
15. V. A. Kuzmin, A. P. Darmanyan, Study of sterically hindered short-lived isomers of polymethine dyes by laser photolysis. *Chem. Phys. Lett.* **54**, 159–163 (1978).
16. C. Eggeling, J. Widengren, R. Rigler, C. A. Seidel, Photobleaching of fluorescent dyes under conditions used for single-molecule detection: Evidence of two-step photolysis. *Anal. Chem.* **70**, 2651–2659 (1998).

17. C. Eggeling *et al*., Analysis of photobleaching in single-molecule multicolor excitation and Förster resonance energy transfer measurements. *J. Phys. Chem. A* **110**, 2979–2995 (2006).
18. C. Joo, H. Balci, Y. Ishitsuka, C. Buranachai, T. Ha, Advances in single-molecule fluorescence methods for molecular biology. *Annu. Rev. Biochem.* **77**, 51–76 (2008).
19. M. F. Juette *et al*., The bright future of single-molecule fluorescence imaging. *Curr. Opin. Chem. Biol.* **20**, 103–111 (2014).
20. R. E. Benesch, R. Benesch, Enzymatic removal of oxygen for polarography and related methods. *Science* **118**, 447–448 (1953).
21. C. E. Aitken, R. A. Marshall, J. D. Puglisi, An oxygen scavenging system for improvement of dye stability in single-molecule fluorescence experiments. *Biophys. J.* **94**, 1826–1835 (2008).
22. M. Swoboda *et al*., Enzymatic oxygen scavenging for photostability without pH drop in single-molecule experiments. *ACS Nano* **6**, 6364–6369 (2012).
23. E. A. Lemke *et al*., Microfluidic device for single-molecule experiments with enhanced photostability. *J. Am. Chem. Soc.* **131**, 13610–13612 (2009).
24. C. Grewer, H.-D. Brauer, Mechanism of the triplet-state quenching by molecular oxygen in solution. *J. Phys. Chem.* **98**, 4230–4235 (1994).
25. M. E. Dailey, E. Manders, D. R. Soll, M. Terasaki, *Handbook of Biological Confocal Microscopy*, J. B. Pawley, Ed. (Springer, Boston, MA, 2006), pp. 381–403.
26. G. Dormán, G. D. Prestwich, Benzophenone photophores in biochemistry. *Biochemistry* **33**, 5661–5673 (1994).
27. G. W. Preston, A. J. Wilson, Photo-induced covalent cross-linking for the analysis of biomolecular interactions. *Chem. Soc. Rev.* **42**, 3289–3301 (2013).
28. I. Rasnik, S. A. McKinney, T. Ha, Nonblinking and long-lasting single-molecule fluorescence imaging. *Nat. Methods* **3**, 891–893 (2006).
29. J. Widengren, A. Chmyrov, C. Eggeling, P.-A. Löfdahl, C. A. M. Seidel, Strategies to improve photostabilities in ultrasensitive fluorescence spectroscopy. *J. Phys. Chem. A* **111**, 429–440 (2007).
30. J. Vogelsang *et al*., A reducing and oxidizing system minimizes photobleaching and blinking of fluorescent dyes. *Angew. Chem. Int. Ed. Engl.* **47**, 5465–5469 (2008).
31. R. Dave, D. S. Terry, J. B. Munro, S. C. Blanchard, Mitigating unwanted photophysical processes for improved single-molecule fluorescence imaging. *Biophys. J.* **96**, 2371–2381 (2009).
32. T. Cordes, A. Maiser, C. Steinhauer, L. Schermelleh, P. Tinnefeld, Mechanisms and advancement of antifading agents for fluorescence microscopy and single-molecule spectroscopy. *Phys. Chem. Chem. Phys.* **13**, 6699–6709 (2011).
33. M. Heilemann, E. Margeat, R. Kasper, M. Sauer, P. Tinnefeld, Carbocyanine dyes as efficient reversible single-molecule optical switch. *J. Am. Chem. Soc.* **127**, 3801–3806 (2005).
34. G. T. Dempsey *et al*., Photoswitching mechanism of cyanine dyes. *J. Am. Chem. Soc.* **131**, 18192–18193 (2009).
35. J. L. Alejo, S. C. Blanchard, O. S. Andersen, Small-molecule photostabilizing agents are modifiers of lipid bilayer properties. *Biophys. J.* **104**, 2410–2418 (2013).
36. R. B. Altman *et al*., Cyanine fluorophore derivatives with enhanced photostability. *Nat. Methods* **9**, 68–71 (2011).
37. R. B. Altman *et al*., Enhanced photostability of cyanine fluorophores across the visible spectrum. *Nat. Methods* **9**, 428–429 (2012).
38. Q. Zheng *et al*., Electronic tuning of self-healing fluorophores for live-cell and single-molecule imaging. *Chem. Sci.* **8**, 755–762 (2017).
39. P. Tinnefeld, T. Cordes, "Self-healing" dyes: Intramolecular stabilization of organic fluorophores. *Nat. Methods* **9**, 426–427 (2012).
40. S. C. Blanchard, Reply to "Self-healing' dyes: Intramolecular stabilization of organic fluorophores. *Nat. Methods* **9**, 427–428 (2012).
41. Q. Zheng *et al*., On the mechanisms of cyanine fluorophore photostabilization. *J. Phys. Chem. Lett.* **3**, 2200–2203 (2012).
42. Q. Zheng *et al*., Intra-molecular triplet energy transfer is a general approach to improve organic fluorophore photostability. *Photochem. Photobiol. Sci.* **15**, 196–203 (2016).
43. Q. Zheng, S. Jockusch, Z. Zhou, S. C. Blanchard, The contribution of reactive oxygen species to the photobleaching of organic fluorophores. *Photochem. Photobiol.* **90**, 448–454 (2014).
44. J. H. M. van der Velde *et al*., Mechanism of intramolecular photostabilization in self-healing cyanine fluorophores. *ChemPhysChem* **14**, 4084–4093 (2013).
45. J. H. M. van der Velde *et al*., The power of two: Covalent coupling of photostabilizers for fluorescence applications. *J. Phys. Chem. Lett.* **5**, 3792–3798 (2014).
46. J. H. M. van der Velde *et al*., A simple and versatile design concept for fluorophore derivatives with intramolecular photostabilization. *Nat. Commun.* **7**, 10144 (2016). Correction in: *Nat. Commun.* **9**, 16232 (2018).
47. T. C. Bruice, U. K. Pandit, The effect of geminal substitution ring size and rotamer distribution on the intramolecular nucleophilic catalysis of the hydrolysis of monophenyl esters of dibasic acids and the solvolysis of the intermediate anhydrides. *J. Am. Chem. Soc.* **82**, 5858–5865 (1960).
48. F. C. Lightstone, T. C. Bruice, Ground state conformations and entropic and enthalpic factors in the efficiency of intramolecular and enzymatic reactions. 1. Cyclic anhydride formation by substituted glutarates, succinate, and 3,6-endoxo-Δ^4 -tetrahydrophthalate monophenyl esters. *J. Am. Chem. Soc.* **118**, 2595–2605 (1996).
49. P. J. Forward, A. A. Gorman, I. Hamblett, "Nonvertical" triplet energy transfer to cyclooctatetraene: Support for the single-bond torsion mechanism. *J. Chem. Soc. Chem. Commun.* **1993**, 250–251 (1993).
50. L. A. Paquette, The current view of dynamic change within cyclooctatetraenes. *Acc. Chem. Res.* **26**, 57–62 (1993).
51. L. M. Frutos, O. Castano, J. L. Andres, M. Merchan, A. U. Acuna, A theory of non-vertical triplet energy transfer in terms of accurate potential energy surfaces: The transfer reaction from pi,pi* triplet donors to 1,3,5,7-cyclooctatetraene. *J. Chem. Phys.* **120**, 1208–1216 (2004).
52. N. C. Baird, Quantum organic photochemistry. II. Resonance and aromaticity in the lowest 3.pi.pi.* state of cyclic hydrocarbons. *J. Am. Chem. Soc.* **94**, 4941–4948 (1972).
53. M. Rosenberg, C. Dahlstrand, K. Kilså, H. Ottosson, Excited state aromaticity and antiaromaticity: Opportunities for photophysical and photochemical rationalizations. *Chem. Rev.* **114**, 5379–5425 (2014).
54. F. A. L. Anet, The rate of bond change in cycloöctatetraene. *J. Am. Chem. Soc.* **84**, 671–672 (1962).
55. J. F. M. Oth, Conformational mobility and fast bond shift in the annulenes. *Pure Appl. Chem.* **25**, 573–622 (1971).
56. O. A. El Seoud, W. J. Baader, E. L. Bastos, "Practical chemical kinetics in solution" in *Encyclopedia of Physical Organic Chemistry*, Z. Wang, Ed. (John Wiley, Hoboken, NJ, 2016), vol. 1, pp. 369–436.
57. L. A. Paquette, S. V. Ley, R. H. Meisinger, R. K. Russell, M. Oku, Directed syntheses of the isomeric dimethylcyclooctatetraenes and a study of their polarographic and alkali metal reduction. *J. Am. Chem. Soc.* **96**, 5806–5815 (1974).
58. W. Adam, G. Klug, E.-M. Peters, K. Peters, H. G. von Schnering, Synthesis of endoperoxides derived from cyclooctatetraenes via singlet oxygenation. *Tetrahedron* **41**, 2045–2056 (1985).
59. T. N. Das, K. I. Priyadarshini, Triplet of cyclooctatetraene: Reactivity and properties. *J. Chem. Soc.Faraday Trans.* **90**, 963–968 (1994).
60. M. Levitus, S. Ranjit, Cyanine dyes in biophysical research: The photophysics of polymethine fluorescent dyes in biomolecular environments. *Q. Rev. Biophys.* **44**, 123–151 (2011).
61. R. B. Mujumdar, L. A. Ernst, S. R. Mujumdar, C. J. Lewis, A. S. Waggoner, Cyanine dye labeling reagents: Sulfoindocyanine succinimidyl esters. *Bioconjug. Chem.* **4**, 105–111 (1993).
62. R. Roy, S. Hohng, T. Ha, A practical guide to single-molecule FRET. *Nat. Methods* **5**, 507–516 (2008).
63. E. Lerner *et al*., Toward dynamic structural biology: Two decades of single-molecule Förster resonance energy transfer. *Science* **359**, eaan1133 (2018).
64. U. E. Steiner, *Photodynamic Therapy*, M. H. Abdel-Kader, Ed. (Springer, Berlin, Germany, 2014), pp. 25–58.
65. N. J. Turro, V. Ramamurthy, J. C. Scaiano, *Modern Molecular Photochemistry of Organic Molecules*, (University Science, 2010).
66. P. A. M. Dirac, The quantum theory of the emission and absorption of radiation. *Proc. R. Soc. A* **114**, 243–265 (1927).
67. J. J. Sakurai, J. Napolitano, *Modern Quantum Mechanics*, (Cambridge University Press, 2017).
68. R. O. Jones, Density functional theory: Its origins, rise to prominence, and future. *Rev. Mod. Phys.* **87**, 897–923 (2015).
69. M. F. Juette *et al*., Single-molecule imaging of non-equilibrium molecular ensembles on the millisecond timescale. *Nat. Methods* **13**, 341–344 (2016).
70. R. Y. Tsien, L. Ernst, A. Waggoner, *Handbook of Biological Confocal Microscopy*, J. B. Pawley, Ed. (Springer, Boston, MA, 2006), pp. 338–352.
71. L. C. Zanetti-Domingues, C. J. Tynan, D. J. Rolfe, D. T. Clarke, M. Martin-Fernandez, Hydrophobic fluorescent probes introduce artifacts into single molecule tracking experiments due to non-specific binding. *PLoS One* **8**, e74200 (2013).
72. V. Glembockyte, J. Lin, G. Cosa, Improving the photostability of red- and green-emissive single-molecule fluorophores via Ni^{2+} mediated excited triplet-state quenching. *J. Phys. Chem. B* **120**, 11923–11929 (2016).
73. H. S. Chung, K. McHale, J. M. Louis, W. A. Eaton, Single-molecule fluorescence experiments determine protein folding transition path times. *Science* **335**, 981–984 (2012).
74. V. Muñoz, M. Cerminara, When fast is better: Protein folding fundamentals and mechanisms from ultrafast approaches. *Biochem. J.* **473**, 2545–2559 (2016).
75. F. Sturzenegger *et al*., Transition path times of coupled folding and binding reveal the formation of an encounter complex. *Nat. Commun.* **9**, 4708 (2018).
76. L. A. Campos *et al*., A photoprotection strategy for microsecond-resolution single-molecule fluorescence spectroscopy. *Nat. Methods* **8**, 143–146 (2011).
77. J.-Y. Kim, C. Kim, N. K. Lee, Real-time submillisecond single-molecule FRET dynamics of freely diffusing molecules with liposome tethering. *Nat. Commun.* **6**, 6992 (2015).
78. S. Chino, A. Sakaguchi, R. Yamoto, S. Ferri, K. Sode, Branched-chain amino acid biosensing using fluorescent modified engineered leucine/isoleucine/valine binding protein. *Int. J.Mol. Sci.* **8**, 513–525 (2007).
79. G. A. Fitzgerald *et al*., Quantifying secondary transport at single-molecule resolution. *Nature* **575**, 528–534 (2019).
80. A. Hoffmann *et al*., Quantifying heterogeneity and conformational dynamics from single molecule FRET of diffusing molecules: Recurrence analysis of single particles (RASP). *Phys. Chem. Chem. Phys.* **13**, 1857–1871 (2011).
81. S. A. McKinney, C. Joo, T. Ha, Analysis of single-molecule FRET trajectories using hidden Markov modeling. *Biophys. J.* **91**, 1941–1951 (2006).
82. I. V. Gopich, A. Szabo, Single-molecule FRET with diffusion and conformational dynamics. *J. Phys. Chem. B* **111**, 12925–12932 (2007).
83. P. J. Bosch *et al*., Evaluation of fluorophores to label SNAP-tag fused proteins for multicolor single-molecule tracking microscopy in live cells. *Biophys. J.* **107**, 803–814 (2014).
84. J. B. Grimm *et al*., A general method to fine-tune fluorophores for live-cell and in vivo imaging. *Nat. Methods* **14**, 987–994 (2017).
85. L. Wang *et al*., A general strategy to develop cell permeable and fluorogenic probes for multicolour nanoscopy. *Nat. Chem.* **12**, 165–172 (2020).
86. G. Lukinavičius *et al*., Fluorescent dyes and probes for super-resolution microscopy of microtubules and tracheoles in living cells and tissues. *Chem. Sci.* **9**, 3324–3334 (2018).